ATLAS CONF Note

ATLAS-CONF-2023-036

18th July 2023

Measurement of the Higgs boson mass with $H \to \gamma\gamma$ decays in 140 fb^{-1} of $\sqrt{s}$ = 13 TeV pp collisions with the ATLAS detector

The ATLAS Collaboration

The mass of the Higgs boson is measured in the $H \to \gamma\gamma$ decay channel, exploiting the high resolution of the invariant mass of photon pairs reconstructed from the decays of Higgs bosons produced in proton-proton collisions at a centre-of-mass energy $\sqrt{s}$ = 13 TeV. The dataset was collected between 2015 and 2018 by the ATLAS detector at the Large Hadron Collider, and corresponds to an integrated luminosity of 140 fb^{-1}. The measured value of the Higgs boson mass is 125.17 ± 0.11 (stat.) ± 0.09 (syst.) GeV and is based on an improved energy scale calibration for photons whose impact on the measurement is about four times smaller than in the previous publication. A combination with the corresponding measurement using 7 and 8 TeV pp collision ATLAS data results in a Higgs boson mass measurement of 125.22 ± 0.11 (stat.) ± 0.09 (syst.) GeV. With a relative uncertainty of 1.1 per mille, this is currently the most precise measurement of the mass of the Higgs boson from a single decay channel.

ATLAS-CONF-2023-036
19 July 2023

Contents

1 Introduction

After the ATLAS and CMS collaborations discovered in 2012 [1, 2] at the Large Hadron Collider (LHC) a particle H with properties consistent with those of the Higgs boson in the Standard Model (SM) of particle physics, the precise determination of its mass has become one of the primary goals in their physics programmes. The Higgs boson mass m_H is a fundamental parameter of the SM and, with the Higgs boson self-coupling, the only unknown parameter of the scalar sector of the Standard Model prior to the Higgs boson discovery. Its measurement is of paramount importance for several reasons. Firstly, its value determines the Higgs boson production rates and decay branching ratios [3]. It is also the value assumed by the experimental collaborations when estimating acceptances, efficiencies and the signal models used in their analyses and to report their measured rates. The knowledge of the Higgs boson mass is therefore mandatory for a coherent test of its coupling structure. Secondly, the Higgs boson mass is one of the inputs in global fits to the measurements of electroweak observables [4]. Knowing its value therefore plays a key role in verifying the internal consistency of the SM, in particular through the interplay between the masses of the top quark and of the W and Higgs bosons. Finally, the stability of the electroweak vacuum and thus the fate of our Universe depend on the value of the Higgs boson mass [5]. By measuring m_H, one can infer whether the Universe is either in a global, and thus stable, minimum-energy state of the Higgs field potential, or in a local, meta-stable one, from which it could decay to the ground state in the future [6].

Measurements of the Higgs boson mass were performed separately by the ATLAS [7] and CMS [8] collaborations using Higgs boson decays to the high-resolution four-lepton (4ℓ, $\ell = e, \mu$) and diphoton ($\gamma\gamma$) final states reconstructed during the first data-taking phase of the LHC (Run 1). The data consisted of 25 fb^{-1} of proton-proton (pp) collisions recorded at centre-of-mass energies $\sqrt{s}$ = 7 and 8 TeV in 2011

and 2012 . The combination of the ATLAS and CMS results led to a measurement of the Higgs boson mass with a relative uncertainty of 0.19%, $m_H = 125.09 \pm 0.24$ GeV [9].

Updated measurements of the Higgs boson mass were performed by both experiments using pp collisions collected at $\sqrt{s} = 13$ TeV between 2015 and 2018 during the second data-taking phase of the LHC (Run 2). Using both $H \to ZZ^* \to 4\ell$ and $H \to \gamma\gamma$ decays selected in a partial Run 2 dataset (36 fb^{-1} of pp collisions recorded before 2017), the ATLAS collaboration measured $m_H = 124.86 \pm 0.27$ GeV [10]. Combined with the ATLAS Run 1 results of Ref. [7], this study led to a Higgs boson mass measurement of $m_H = 124.97 \pm 0.24$ GeV. Using a dataset of equivalent size and both four-lepton and diphoton final states, the CMS collaboration found $m_H = 125.78 \pm 0.26$ GeV [11], whose combination with the Run 1 results of Ref. [8] led to the most precise determination of m_H to-date, with a 0.11% relative uncertainty: $m_H = 125.38 \pm 0.14$ GeV. Recently, the ATLAS collaboration released an updated measurement of m_H using $H \to ZZ^* \to 4\ell$ decays in the full Run 2 dataset [12], consisting of 140 fb^{-1} of pp collisions. The result, $m_H = 124.99 \pm 0.19$ GeV, combined with that of the corresponding analysis using Run 1 data, yields a single-channel Higgs boson mass measurement with a relative uncertainty of 0.14%, $m_H = 124.94 \pm 0.18$ GeV.

In this note, a measurement of the Higgs boson mass in the diphoton channel using the full Run 2 dataset is reported. Compared with that of Ref. [10], the analysis presented here profits from a larger data sample, a new photon reconstruction algorithm with better energy resolution [13], an improved estimation of the photon energy scale with reduced uncertainties [14], and an optimised event classification strategy. The selected events are required to contain two energetic photons fulfilling strict identification and isolation criteria. The invariant mass ($m_{\gamma\gamma}$) distribution of the selected photon pairs exhibits a peak near m_H, arising from resonant Higgs boson decays, over a smoothly falling distribution from background processes mainly due to non-resonant diphoton production. The Higgs boson mass is determined from the position of the peak in data through a profile-likelihood fit to the $m_{\gamma\gamma}$ distribution. Simulated signal and background event samples are used to optimise the analysis criteria, to define the signal and background $m_{\gamma\gamma}$ models used in the fit, and to estimate the impact of the systematic uncertainties in m_H. To increase the sensitivity of the measurement, the selected events are classified into mutually exclusive categories with different diphoton invariant mass resolutions and signal-to-background ratios which are analysed simultaneously. Finally, a combination with the ATLAS Run 1 measurement [9] is performed.

The note is organised as follows. The ATLAS detector is described briefly in Section 2. The data and simulated samples used in the analysis are summarised in Section 3. The photon reconstruction and the event selection and classification are discussed in Section 4. The statistical tools used for the measurement and the methods to assess the systematic uncertainties are presented in Sections 5 and 6, leading to the results described in Section 7. The conclusions of this study are summarised in Section 8.

2 The ATLAS detector

The ATLAS experiment [15] at the LHC is a multipurpose particle detector with a forward–backward symmetric cylindrical geometry and a near 4π coverage in solid angle.[1] It consists of an inner tracking

[1] ATLAS uses a right-handed coordinate system with its origin at the nominal interaction point (IP) in the centre of the detector and the z-axis along the beam pipe. The x-axis points from the IP to the centre of the LHC ring, and the y-axis points upwards. Cylindrical coordinates (r, ϕ) are used in the transverse plane, ϕ being the azimuthal angle around the z-axis. The pseudorapidity is defined in terms of the polar angle θ as $\eta = -\ln\tan(\theta/2)$. Angular distance is measured in units of $\Delta R \equiv \sqrt{(\Delta\eta)^2 + (\Delta\phi)^2}$. The transverse energy is defined as $E_{\mathrm{T}} = E\sin(\theta)$.

detector surrounded by a thin superconducting solenoid providing a 2 T axial magnetic field, electromagnetic and hadron calorimeters, and a muon spectrometer. The inner tracking detector covers the pseudorapidity range $|\eta| < 2.5$. It consists of silicon pixel, silicon microstrip, and transition radiation tracking detectors. Lead/liquid-argon (LAr) sampling calorimeters provide electromagnetic (EM) energy measurements with high granularity. A steel/scintillator-tile hadron calorimeter covers the central pseudorapidity range ($|\eta| < 1.7$). The endcap and forward regions are instrumented with LAr calorimeters for both the EM and hadronic energy measurements up to $|\eta| = 4.9$. The muon spectrometer surrounds the calorimeters and is based on three large superconducting air-core toroidal magnets with eight coils each. The field integral of the toroids ranges between 2.0 and 6.0 T m across most of the detector. The muon spectrometer includes a system of precision tracking chambers and fast detectors for triggering.

A two-level trigger system is used to select events. The first-level trigger is implemented in hardware and uses a subset of the detector information to accept events at a rate below 100 kHz. This is followed by a software-based trigger that reduces the accepted event rate to 1 kHz on average depending on the data-taking conditions. An extensive software suite [16] is used in the reconstruction and analysis of real and simulated data, in detector operations, and in the trigger and data acquisition systems of the experiment.

3 Data and simulation samples

3.1 Data

The measurement relies on the full pp collision dataset collected at $\sqrt{s} = 13$ TeV by the ATLAS detector during the LHC Run 2. Events were recorded using unprescaled diphoton and single-photon triggers [17]. The photon transverse momentum thresholds were 35 GeV and 25 GeV for the diphoton triggers throughout the whole Run 2, and 120 (140) GeV for single-photon triggers in 2015–2016 (2017–2018). Shower-shape requirements looser than those used in the off-line analysis were applied to the photon candidates at the trigger level. The integrated luminosity of the data set after trigger and data-quality requirements [18] is 140.1 ± 1.2 fb^{-1} [19, 20]. The efficiency of the trigger system for signal events passing the full selection is close to 100% [17].

3.2 Simulation samples

Monte Carlo simulated event samples of Higgs bosons produced by the pp collisions and decaying to diphotons, as well as of the main background processes for the same final state, were produced with the setup described in Ref. [21]. Simulated hard-scattering events were overlaid with simulated inelastic proton–proton events generated with Pythia 8.1 [22], to model the effect of multiple "pile-up" interactions in the same and neighbouring bunch crossings.

Signal samples were produced for the main Higgs boson production modes: gluon-gluon fusion (ggF), vector-boson fusion (VBF), and associated production with a vector boson (VH, $V = W, Z$), a top-quark pair ($t\bar{t}H$), a bottom-quark pair ($b\bar{b}H$) or a single top quark (tH). Signal event samples (except tH) were produced with the Powheg [23] (MadGraph5_aMC@NLO [24]) event generator, using matrix element calculations at the highest available order of accuracy in the strong coupling constant α_s, either next-to-next-to-leading order (NNLO, for ggF), next-to-leading order (NLO, for VBF, WH, $q\bar{q} \to ZH$, $t\bar{t}H$,

$b\bar{b}H$ and tH) or leading order (LO, for $gg \to ZH$). The event generators were interfaced to Pythia8.2 [25] for the modelling of the parton shower and the underlying event. In the analysis they are normalised to the integrated luminosity of the data using state-of-the-art Standard Model calculations for the Higgs boson production cross-sections and branching ratios at the hypothesised Higgs boson mass [3]. The generated signal samples were passed through a detailed simulation of the response of the ATLAS detector [26] based on Geant4 [27].

The nominal signal samples were generated assuming a Higgs boson mass of 125 GeV. The Higgs boson width Γ in all signal samples was set to the SM prediction for $m_H = 125$ GeV, $\Gamma = 4.07$ MeV, which is much narrower than the experimental resolution. Systematic uncertainties related to the modelling of the parton shower are studied with alternative samples that were produced using the same matrix-element generator as the nominal ones but with the Herwig 7.1.3 parton shower algorithm [28]. The parameterisations of the expected signal yields and diphoton invariant mass distributions as a function of the Higgs boson mass are obtained through an interpolation of signal samples generated with m_H set to one of the following values: 110, 122, 123, 124, 125, 126, 127, 130 or 140 GeV. The same setup as that of the nominal samples was used.

Background events from non-resonant $pp \to \gamma\gamma + n$ parton ($n \geq 0$) production were also generated, using the Sherpa 2.2.4 event generator [29] with NLO-accurate matrix elements for up to one parton, and leading-order (LO) accurate matrix elements for up to three partons. Due to its large size, the $pp \to \gamma\gamma$ sample was processed by a fast simulation of the ATLAS detector [30], based on a parameterisation of the response of the calorimeter. Since the di-photon background is estimated from the sidebands in the diphoton invariant mass distribution in data, the background simulation is only used to select the background model and the systematic uncertainty associated with this choice, for which the fast simulation was found to be sufficiently accurate.

The effect of the interference between the resonant signal and the non-resonant background diphoton production is studied using simulated event samples of diphoton production including contributions from both processes, produced by either the gg or qg partonic channels, and their interference. The accuracy of the calculations is NLO for the gg-interference and LO for the qg-interference samples. The events were generated using Sherpa 2.2.11 and passed through the Geant4 detector simulation.

4 Event selection and classification

The event reconstruction and selection closely resemble those used by the latest ATLAS measurement of Higgs boson production cross-sections with the diphoton channel using the full Run 2 dataset [21]. The main differences are the use of an updated photon energy calibration [14] with reduced systematic uncertainties, and the classification of events in categories that are optimised to minimise the uncertainty in the measured Higgs boson mass rather than in the Higgs boson production cross-sections.

Compared with the previous mass measurement [10], which used photon candidates reconstructed from a fixed-size cluster of energy deposits in the electromagnetic calorimeter identified by a sliding-window algorithm, this measurement relies on photon candidates that are reconstructed from dynamic, variable-size clusters, called superclusters. The main advantages of this algorithm are an improved reconstruction efficiency and energy measurement of converted photons ($\gamma \to e^+e^-$), and a reduced misclassification rate of unconverted photons as converted photon candidates [13].

The photon energy is determined from the signals deposited in the electromagnetic calorimeter after the calibration scheme detailed in Ref. [14]. The photon direction is calculated from the positions of the supercluster and of the pp collision vertex that is chosen, among the reconstructed primary vertex candidates, by a neural-network (NN) algorithm [31]. The NN inputs are the directions of the two p_{T}-leading photon candidates in the event, determined only from the longitudinal sampling of the calorimeter and conversion vertices, and vertex candidate information such as the transverse momenta and directions of the associated tracks.

The selection retains events with at least two photon candidates with pseudorapidity in the range $|\eta| < 1.37$ or $1.52 < |\eta| < 2.37$, passing *tight* identification and *loose* isolation criteria [13], matched to the on-line photon candidates that passed the trigger selection. Events are kept if the p_{T}-leading and subleading photon candidates have invariant mass $m_{\gamma\gamma}$ in the range 105–160 GeV and transverse momenta that are greater than 0.35 and 0.25 times $m_{\gamma\gamma}$, respectively. When more than two photon candidates pass the previous requirements, only the p_{T}-leading and subleading candidates are considered for further analysis.

About 1.2 million events in the data pass the selection. The expected efficiency for the signal for $m_H = 125$ GeV is close to 36%, leading to an expected signal yield of about 6200 events.

To increase the precision of the mass measurement, the selected events are classified into 14 categories with different signal-to-background ratios, diphoton invariant mass resolutions and photon energy-scale uncertainties. The observables and the thresholds used to define the categories are optimised by minimising the expected total Higgs boson mass uncertainty for $m_H = 125.09$ GeV using a simplified version of the maximum likelihood fit described in the next section, including the statistical uncertainties and the dominant systematic uncertainties from the photon energy scale calibration. The events are assigned to one of the mutually exclusive categories based on the following observables:

- the number of reconstructed converted photon candidates: events with no photon conversion candidates ("U"-type events) are considered separately from events with one or two $\gamma \rightarrow e^+e^-$ candidates ("C"-type events).
- the absolute value of the pseudorapidity $|\eta_{S2}|$ of each of the two energy clusters reconstructed in the electromagnetic calorimeter and associated with the photon candidates. The pseudorapidity η_{S2} is determined from the position of the barycenter of the cluster in the second sampling layer of the calorimeter and from the origin of the ATLAS coordinate system. Both U-type and C-type events are split in three subsamples: "central barrel" (both photons with $|\eta_{S2}| < 0.8$), "outer-barrel" (both photons with $|\eta_{S2}| < 1.37$, among which at least one photon with $|\eta_{S2}| \geq 0.8$) and "endcap" events (at least one photon with $1.52 \leq |\eta_{S2}| < 2.37$).
- the magnitude of the component of the diphoton transverse momentum that is orthogonal to the thrust-axis $\hat{t} = \frac{\vec{p}_{\mathrm{T}}^{\gamma_1} - \vec{p}_{\mathrm{T}}^{\gamma_2}}{|\vec{p}_{\mathrm{T}}^{\gamma_1} - \vec{p}_{\mathrm{T}}^{\gamma_2}|}$: $p_{\mathrm{Tt}}^{\gamma\gamma} = |\vec{p}_{\mathrm{T}}^{\gamma\gamma} \times \hat{t}|$. Low ($p_{\mathrm{Tt}}^{\gamma\gamma} < 70$ GeV), medium (70 GeV$< p_{\mathrm{Tt}}^{\gamma\gamma} < 130$ GeV) and high ($p_{\mathrm{Tt}}^{\gamma\gamma} > 130$ GeV) $p_{\mathrm{Tt}}^{\gamma\gamma}$ categories are defined for U-type and C-type central-barrel and outer-barrel events.

For each category, the narrowest diphoton invariant mass window, with half-width denoted as $\sigma_{90}^{\gamma\gamma}$, containing 90% of the signal events is listed in Table 1. The expected signal (S_{90}) and background (B_{90}) yields in each category in that interval are also reported, where B_{90} is determined from the integral in the interval of an exponentiated second-order polynomial function fitted to the data $m_{\gamma\gamma}$ distribution after excluding the $120 < m_{\gamma\gamma} < 130$ GeV interval. The table also indicates the expected values of the fraction of

Table 1: The expected signal (S_{90}) and background (B_{90}) yields, fraction of signal events with respect to the total (f_{90}), and signal significance (Z_{90}) in a diphoton invariant mass window whose half-width $\sigma_{90}^{\gamma\gamma}$ is chosen in such a way that it is the narrowest interval containing 90% of signal events. All numbers are given for each analysis category and for the inclusive case.

Category	$\sigma_{90}^{\gamma\gamma}$ [GeV]	S_{90}	B_{90}	f_{90} [%]	Z_{90}
U, Central-barrel, high $p_{\mathrm{Tt}}^{\gamma\gamma}$	1.88	42	65	39.1	4.7
U, Central-barrel, medium $p_{\mathrm{Tt}}^{\gamma\gamma}$	2.34	102	559	15.4	4.2
U, Central-barrel, low $p_{\mathrm{Tt}}^{\gamma\gamma}$	2.63	837	13226	6.0	7.2
U, Outer-barrel, high $p_{\mathrm{Tt}}^{\gamma\gamma}$	2.16	31	83	27.4	3.3
U, Outer-barrel, medium $p_{\mathrm{Tt}}^{\gamma\gamma}$	2.63	108	981	9.9	3.4
U, Outer-barrel, low $p_{\mathrm{Tt}}^{\gamma\gamma}$	3.00	869	22919	3.7	5.7
U, Endcap	3.33	759	29383	2.5	4.4
C, Central-barrel, high $p_{\mathrm{Tt}}^{\gamma\gamma}$	2.10	26	44	37.3	3.6
C, Central-barrel, medium $p_{\mathrm{Tt}}^{\gamma\gamma}$	2.62	62	389	13.8	3.1
C, Central-barrel, low $p_{\mathrm{Tt}}^{\gamma\gamma}$	3.00	508	9726	5.0	5.1
C, Outer-barrel, high $p_{\mathrm{Tt}}^{\gamma\gamma}$	2.56	34	103	25.0	3.2
C, Outer-barrel, medium $p_{\mathrm{Tt}}^{\gamma\gamma}$	3.20	114	1353	7.8	3.1
C, Outer-barrel, low $p_{\mathrm{Tt}}^{\gamma\gamma}$	3.71	914	30121	2.9	5.2
C, Endcap	4.04	1249	52160	2.3	5.5
Inclusive	3.32	5653	128774	4.2	15.6

signal events $f_{90} = \frac{S_{90}}{S_{90}+B_{90}}$, and the counting signal significance $Z_{90} = \sqrt{2\left((S_{90}+B_{90})\ln\left(1+\frac{S_{90}}{B_{90}}\right)-S_{90}\right)}$ [32].

The invariant mass resolution $\sigma_{90}^{\gamma\gamma}$ of C-type events is 10–20% worse than for U-type ones due to asymmetric $\gamma \to e^+e^-$ conversions producing an electron or a positron of low energy, and to bremsstrahlung photons emitted by the e^+e^- pair. In both cases, such soft electrons, positrons or bremsstrahlung photons can escape the supercluster and the calibration procedure might not be fully efficient in recovering the energy of the original photon. The resolution is 6–20% better in central-barrel categories than in the corresponding outer-barrel categories due to the smaller amount of material upstream of the electromagnetic calorimeter in the central region of the detector. Events with high $p_{\mathrm{Tt}}^{\gamma\gamma}$ have about 15–20% (30%) better $m_{\gamma\gamma}$ resolution than events with medium (low) $p_{\mathrm{Tt}}^{\gamma\gamma}$, due to the worse photon energy resolution at lower photon transverse momentum. The signal fraction f_{90} also depends on the same quantities: it is larger for U-type and for central-barrel events, and increases with $p_{\mathrm{Tt}}^{\gamma\gamma}$ since the main background process, continuum diphoton production predominantly arising from t-channel $q\bar{q} \to \gamma\gamma$ and $gg \to \gamma\gamma$ scattering, has a softer $p_{\mathrm{Tt}}^{\gamma\gamma}$ spectrum than the signal. The photon energy scale uncertainty is smaller for C-type and central-barrel events compared to U-type and outer-barrel or endcap events; it increases with $p_{\mathrm{Tt}}^{\gamma\gamma}$ due to uncertainties in the linearity of the response and in the extrapolation to photons of the energy scale calibration, mainly determined using electron and positron candidates of relatively low transverse momentum from $Z \to e^+e^-$ decays.

The chosen categorisation leads to a reduction of about 17% of the expected uncertainty in m_H from statistical and photon energy scale systematic uncertainties with respect to a measurement based on the inclusive sample passing the event selection, and of 6% compared with the use of the event classification strategy of Ref. [10]. Compared with the 101 event categories developed in Ref. [21] for the measurement of

the Higgs boson production-mode cross-sections times branching ratio to diphotons using the same dataset, the 14 categories used in this note lead to a small increase (+3%) of the expected statistical uncertainty and to a larger decrease (−14%) of the systematic uncertainty in m_H, yielding an overall expected reduction (−3%) of the total uncertainty.

5 Mass measurement procedure

The Higgs boson mass m_H is measured using the statistical methods described in Ref. [10]. The diphoton invariant mass distribution of the data is used to define a likelihood function L depending on m_H and on a certain number of additional parameters $\boldsymbol{\theta}$ describing the signal and background normalisations, their $m_{\gamma\gamma}$ models, and corresponding systematic uncertainties. The profile likelihood ratio [32, 33] is then:

$$\Lambda(m_H) = \frac{L\big(m_H, \hat{\hat{\boldsymbol{\theta}}}(m_H)\big)}{L\big(\hat{m}_H, \hat{\boldsymbol{\theta}}\big)}, \tag{1}$$

where $\hat{\boldsymbol{\theta}}$ and $\hat{m}_H$ denote the values of the parameters that maximise the likelihood function L, while $\hat{\hat{\boldsymbol{\theta}}}(m_H)$ represent the values of the parameters $\boldsymbol{\theta}$ that maximise L for a given value of the parameter m_H. A numerical fit procedure determines the central value $\hat{m}_H$ of the measurement and its 68% confidence interval, defined by all values of m_H for which $-2\ln\Lambda(m_H) < 1$. The fit uses the event counts in 25 MeV-wide bins of the $m_{\gamma\gamma}$ distribution in each category.

The likelihood function L is computed from the product of individual likelihood functions for the observed diphoton invariant mass spectra in each category, and of distributions representing auxiliary measurements that constrain the nuisance parameters associated with the systematic uncertainties. The model assumes that the observed distribution arises from the sum of a signal and a background component, whose shape and normalisation are inferred from the data themselves, with some input from the simulation.

The $m_{\gamma\gamma}$ distribution of the signal in each category is found to be properly described, for any value of the Higgs boson mass in the range [110, 140] GeV, by a double-sided Crystal-Ball [34] probability density function, *i.e.* a function with a Gaussian core and power-law tails. The parameters $(\alpha_\pm, n_\pm)$ describing the tails of the model do not depend on m_H, while the parameters μ_{CB} and σ_{CB} related to the peak position and the resolution of the core Gaussian component scale linearly with m_H. The nominal values of the signal shape parameters in each category are determined by a simultaneous fit to the simulated diphoton invariant mass spectra in that category at different m_H hypotheses. As a cross-check, the fit is repeated after removing the $m_H = 125$ GeV distribution from the input, and the signal model extrapolated to $m_H = 125$ GeV is then compared to the model determined from a fit to the $m_H = 125$ GeV simulated signal events. Good agreement is observed. The nominal signal model for a Higgs boson mass $m_H = 125$ GeV for the categories with the best and worst expected resolutions are shown in Figure 1.

The normalisations of the signal, one for each category c, are free parameters of the fit and are expressed as the product of a per-category signal-strength factor μ_c and of the expected number S_c of Higgs boson events in the same analysis region. The expected signal yield S_c is determined from the integrated luminosity, the SM values of the Higgs boson cross-section and $H \to \gamma\gamma$ branching ratio, and the selection efficiency of the category predicted by the simulation. The dependence of S_c on m_H in each category c is modelled with a second-order polynomial whose parameters are determined by a fit to the expected yields in that category calculated for nine discrete values of m_H between 110 and 140 GeV using the simulated signal samples described in Section 3.

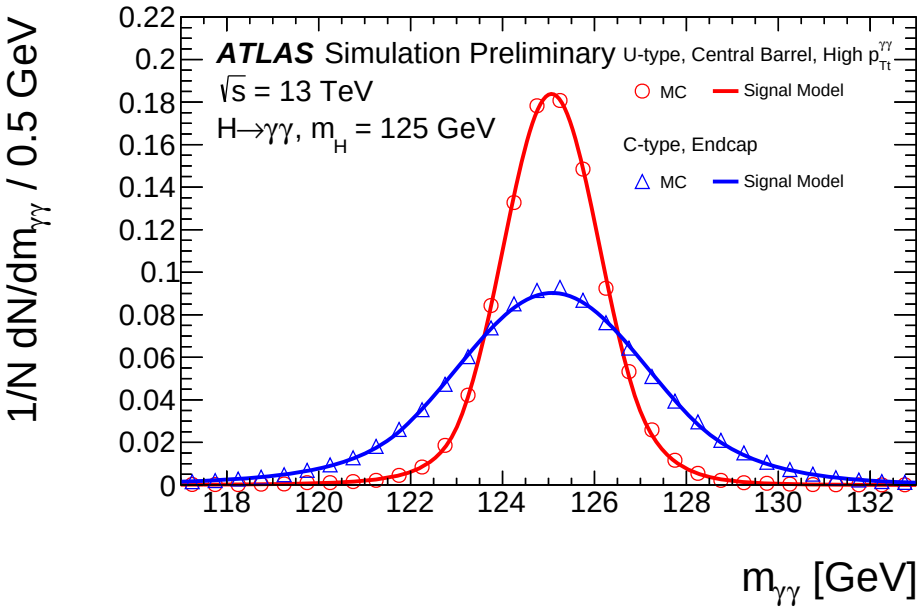

Figure 1: Invariant mass distributions of simulated $H \to \gamma\gamma$ events reconstructed in the categories with the best (U-type, central-barrel, high-$p_{\mathrm{Tt}}^{\gamma\gamma}$: open circles) and the worst (C-type, endcap: open squares) experimental resolutions. The signal model derived from a fit of the simulated events is superimposed (solid lines).

The background $m_{\gamma\gamma}$ distribution in each category is represented by either an exponential function, a power-law function or an exponentiated second-order polynomial. The background model is chosen in an empirical way [21] based on the results of the fits to the diphoton invariant mass distribution of a background template with a model with free parameters for the signal and background yields. The background template is obtained by summing the $m_{\gamma\gamma}$ distributions of simulated non-resonant diphoton events and of data samples enriched in photon+jet and dijet events. The photon+jet and di-jet enriched samples are obtained using a selection similar to that of the previous section, with the exception that one or both photon candidates are required to fail the nominal identification and isolation criteria while passing looser ones. The three distributions are normalised to the yields of the respective contributions estimated *in situ*. Among all considered background models whose χ^2 probability is greater than 1% when fitted to the background template, and for which the fitted signal yield ("spurious signal") is below 10% of the expected signal yield, one selects the one with the least degrees of freedom. The value of the 10% threshold is chosen in such a way that the spurious signal, considered as a systematic uncertainty in the signal yield, is small compared to the statistical uncertainty. The background yield in each category and the parameters describing the shape of the background model are free parameters of the likelihood function.

Systematic uncertainties and their correlations are modelled by including, among the parameters $\boldsymbol{\theta}$, nuisance parameters described by likelihood functions associated with the estimate of the corresponding effect. The statistical uncertainty of m_H is estimated by determining the confidence interval when all nuisance parameters associated to systematic uncertainties are fixed to their best-fit values, while all remaining parameters are left unconstrained. The total systematic uncertainty is estimated by subtracting in quadrature the statistical uncertainty from the total uncertainty.

Compared with the previous measurement, the expected statistical uncertainty on m_H of 120 MeV is reduced by a factor 2.1, due to the dataset being four times larger and to the improved photon reconstruction

algorithm and event classification.

6 Systematic uncertainties

The main sources of systematic uncertainty in m_H are the uncertainties in the photon energy scale, the uncertainty from the background modelling and the effect of the interference between the signal and the $\gamma\gamma$ continuum background. They are described, together with their expected pre-fit impact on m_H, in the following.

The photon energy scale uncertainty is modelled by 67 independent components. The effect of every component is evaluated for each analysis category by comparing the nominal signal MC diphoton invariant mass distribution with the one obtained by varying the energy of each photon by the uncertainty under study. The shifts induced in the peak parameters μ_{CB} of the Crystal-Ball signal models are then included as nuisance parameters in the likelihood function, fully correlated among the categories. The 67 independent sources of uncertainty in the photon energy scale can be classified roughly in four main groups. The first group ($Z \to e^+e^-$ *calibration*) is related to the determination of the η-dependent energy scale factors for electrons and positrons from Z boson decays, effectively constraining their energy scale for a transverse energy $E_{\mathrm{T}} \approx 45$ GeV. The second class (E_{T}-*dependent electron energy scale*) includes uncertainties in the E_{T}-dependence of the energy scale from sources such as the calorimeter readout non-linearity, the calorimeter layer inter-calibration, and the amount of material upstream of the calorimeter. The third set ($e^{\pm} \to \gamma$ *extrapolation*) includes the uncertainties in the extrapolation of the energy scale from electrons to photons, arising for instance from a potential mismodelling of the differences in the lateral shower development in the calorimeter between electrons and photons. Finally, the fourth group (*conversion modelling*) collects the uncertainties related to the accuracy of the photon conversion modelling in the simulation. Since the simulation-based photon energy calibration [14] is trained and applied separately for unconverted and converted photon candidates, any mismodelling of the conversion reconstruction performance in the simulation may affect the calibrated photon energy scale.

The results presented in this note profit from a new auxiliary measurement (*linearity fit*) of the dependence of the data-to-MC electron energy scale corrections as a function of the electron E_{T}. In the photon energy scale calibration used in the previous Higgs boson mass measurement [10], only η-dependent energy scale factors were derived from 2015–2016 data by comparing the position of the peak of the invariant mass distribution of e^+e^- pairs from Z boson decays to that predicted by the simulation. The possible E_{T}-dependence of the data-to-MC energy scale correction was accounted for as a systematic uncertainty, arising from the various sources belonging to the E_{T}-dependent electron energy scale group, calculated as described in Ref. [35]. The new approach used in Ref. [14] exploits the larger sample of $Z \to e^+e^-$ decays collected in 2015–2018 to derive residual data-to-MC energy scale factors in bins of electron transverse energy within broad η regions. The measurement of these additional scale factors is used to constrain the E_{T}-dependent electron energy scale systematic uncertainties. The additional constraints and correlation of the systematic uncertainties from the linearity fit are propagated to the Higgs boson mass measurement by implementing in the likelihood function a multivariate Gaussian constraint term whose covariance is that returned by the linearity fit. The impact of the photon energy scale systematic uncertainties including the effect of the linearity fit was found to be independent of m_H for values of the Higgs boson mass in the range 124–126 GeV, and is expected to be approximately ±83 MeV (60, 43, 30 and 23 MeV respectively from the four individual groups of $Z \to e^+e^-$ calibration, E_{T}-dependent electron energy scale, $e^{\pm} \to \gamma$ extrapolation and conversion modelling uncertainties). With respect to the

results in Ref. [10], a more accurate description in the simulation [13] of the material upstream of the EM calorimeter and the reduced sensitivity to material effects of the new clustering algorithm provided a reduction of the associated systematic uncertainty by a factor close to three. In addition, the larger amount of collected data allowed a more precise study of the $e^{\pm} \to \gamma$ extrapolation procedure [14], and its impact on the expected m_H uncertainty is reduced by a factor larger than three. Furthrmore, the contribution of the E_{T}-dependent electron energy scale uncertainties to the total expected m_H uncertainty has been reduced by a factor of two thanks to more precise dedicated measurements. Finally, the linearity fit constrains the expected uncertainty in the Higgs boson mass from the group of E_{T}-dependent energy scale uncertainties by a further factor of four.

The effect of the interference between the $gg \to H \to \gamma\gamma$ signal and the $gg \to \gamma\gamma$ continuous background and between $gq \to H \to \gamma\gamma$ and $gq \to \gamma\gamma$ is not included in the simulated event samples used to study the nominal signal model. In the Standard Model this interference is expected to change the signal cross-section by 1–2% [36] and to shift the position of the peak in the diphoton invariant mass distribution by a few tens of MeV [37]. The size of this effect is treated as a systematic uncertainty, that is quantified by fitting the nominal signal plus background model to the sum of the expected $m_{\gamma\gamma}$ distributions predicted by the nominal signal and background models and of the $m_{\gamma\gamma}$ distribution in simulated events arising from such interference. The relative differences between the fitted and nominal Higgs boson mass in each analysis category are introduced in the likelihood function as one correlated nuisance parameter affecting coherently the 14 categories. The impact of the interference term on the determination of m_H is expected to be approximately ±24 MeV.

The effect of a possible bias on the measured m_H from a mis-modelling of the continuum background $m_{\gamma\gamma}$ distribution is evaluated by fitting the signal plus background model to the sum of the $m_{\gamma\gamma}$ distribution of the background template described in the previous section and of that predicted by the signal model for $m_H = 125$ GeV. The relative differences between the fitted and nominal Higgs boson mass in each analysis category are then introduced in the likelihood function as 14 additional nuisance parameters, one per category, that are considered uncorrelated among them. The impact of the background modelling uncertainty on the measurement of m_H is expected to be approximately ±18 MeV.

The systematic uncertainty related to the selection of the diphoton production vertex is evaluated on a $Z \to e^+e^-$ control sample. The directions of the selected electrons and positrons and thus their invariant mass are calculated using either the primary vertex candidate with the largest sum of the squared transverse momenta of the associated tracks or using the primary vertex selected by the NN algorithm described in Section 4 when the electron and positron tracks are ignored. The shift between the peak positions of the two e^+e^- invariant mass distributions is evaluated separately in data and simulation. The maximum difference (5 MeV) between the shift observed in data and that observed in the simulation is taken as an additional systematic uncertainty in m_H.

Uncertainties from the chosen parametrisation of the nominal signal model are propagated to the final result by including 14 additional uncorrelated nuisance parameters in the likelihood function. They are determined by fitting the nominal signal plus background model to the sum of the $m_{\gamma\gamma}$ distribution in signal simulated events with m_H =125 GeV and of that predicted by the nominal background model. The impact of the signal modelling uncertainty on the measurement of m_H is expected to be approximately ±5 MeV.

The effect of the photon energy resolution uncertainty is included in the signal model as five nuisance parameters that affect the resolution parameter σ_{CB} of the Crystal-Ball function and are considered as correlated among categories. The impact of the five independent sources of photon energy resolution uncertainty is evaluated by comparing the nominal signal invariant mass distribution in each category with

the ones obtained by varying the resolution of the energy of each photon according to their uncertainty. The sum in quadrature of the different components of the photon energy resolution uncertainty ranges from 4.5% for C-type, outer-barrel, low $p_{\mathrm{Tt}}^{\gamma\gamma}$ events to 17% for U-type, central-barrel, high $p_{\mathrm{Tt}}^{\gamma\gamma}$ events. The impact of the photon energy resolution uncertainty on m_H is expected to be approximately ±3 MeV.

Yield uncertainties from the Higgs boson branching ratio to diphotons and the integrated luminosity of the data, and uncertainties in the migrations of events between categories from various experimental and theoretical sources are included in the model. Experimental uncertainties in the efficiency of photon conversion reconstruction, photon identification, isolation and trigger, as well as in the impact of the modelling of pile-up in the simulation are considered. Theoretical uncertainties that are taken into account are those in the signal production cross-sections, in the modelling of the underlying event and of the parton shower, in the value of the strong coupling constant and in the parton distribution functions of the proton. All the uncertainties described in this paragraph are included in the fit although their expected impact on the measurement of m_H was found to be below 1 MeV.

In summary, compared to the previous publication based on 36 fb^{-1} of ATLAS Run 2 data, the improvements in the photon energy calibration of Ref. [14] and the optimised event classification, lead to a four-fold reduction of the expected value of the dominant systematic uncertainty in m_H from the photon energy scale and resolution, from 320 MeV to 80 MeV, and a similar reduction of the total expected systematic uncertainty, from 330 MeV to 90 MeV.

7 Results

The $m_{\gamma\gamma}$ distribution of the data, overlaid with the sum of the signal and background models corresponding to the maximum-likelihood estimates of the parameters of the likelihood function, is shown in Figure 2. All event categories are included. For illustration purposes, events in each category are weighted by a factor $\ln(1 + S_{90}^{\mathrm{obs}}/B_{90}^{\mathrm{obs}})$, where S_{90}^{obs} and B_{90}^{obs} are the fitted signal and background yields in the smallest $m_{\gamma\gamma}$ interval containing 90% of the signal.

The profile likelihood ratio as a function of m_H is shown in Figure 3(a). The value of the Higgs boson mass determined from the profile likelihood ratio of Eq. (1) fitted to the diphoton invariant mass distribution in data is:

$$m_H = 125.17 \pm 0.11(\mathrm{stat.}) \pm 0.09(\mathrm{syst.})\ \mathrm{GeV} = 125.17 \pm 0.14\ \mathrm{GeV}. \tag{2}$$

The statistical and systematic uncertainties are in good agreement with the values of 120 MeV and 90 MeV expected for a SM Higgs boson with the observed mass. The main sources of observed systematic uncertainty in the measurement are summarised in Table 2.

The signal strength μ_c in each category c is compatible with the SM prediction $\mu_c = 1$, with a maximum difference at the level of 2.2 standard deviations (σ) for the C-type, Central-barrel, medium-$p_{\mathrm{Tt}}^{\gamma\gamma}$ category. The global significance of this deviation, taking into account a trial factor of 14, is less than one σ. The best-fit m_H values for the individual categories are in good agreement with each other, with a global p-value of 8%. If the same signal strength μ is used for each category, the central value of m_H is shifted by −35 MeV, and the fitted value of μ is in agreement with the SM prediction within 1.4 standard deviations. If the signal $m_{\gamma\gamma}$ model is modified to account for the expected shift induced by the interference with non-resonant background diphoton production, the measured value of the Higgs boson mass is increased by approximately 26 MeV.

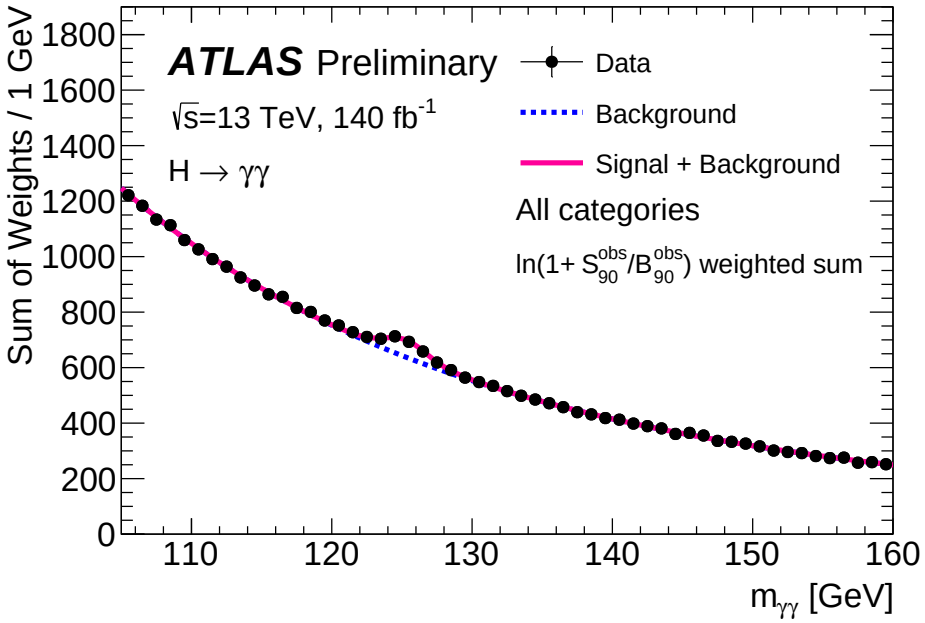

Figure 2: Diphoton invariant mass distribution of all selected data events (black dots with error bars), overlaid with the result of the fit (solid red line). Both for data and for the fit, each category is weighted by a factor $\ln(1 + S_{90}^{\text{obs}}/B_{90}^{\text{obs}})$, where S_{90}^{obs} and B_{90}^{obs} are the fitted signal and background yields in the smallest $m_{\gamma\gamma}$ interval containing 90% of the expected signal. The dotted line describes the background component of the model.

Table 2: Main sources of observed systematic uncertainty in the m_H measurement with Run 2 data.

Source	Systematic uncertainty in m_H [MeV]
Photon energy scale	±83
$Z \to e^+e^-$ calibration	±59
E_{T}-dependent electron energy scale	±44
$e^{\pm} \to \gamma$ extrapolation	±30
Conversion modelling	±24
Signal-background interference	±26
Resolution	±15
Background model	±14
Selection of the diphoton production vertex	±5
Signal model	±1
Total	±90

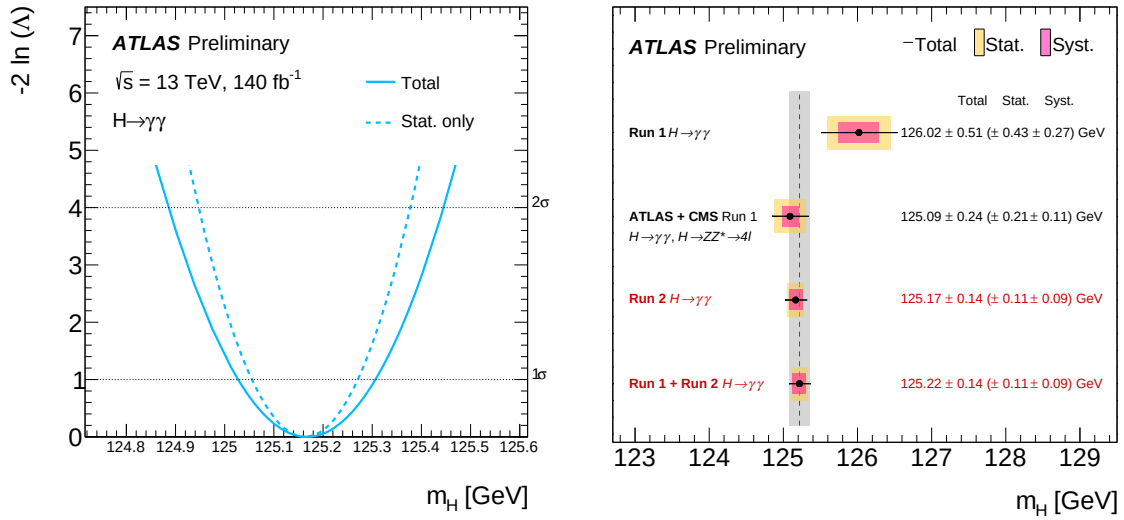

(a) (b)

Figure 3: (a) Value of $-2\ln\Lambda$ as a function of m_H for the combined fit to all $H \to \gamma\gamma$ categories. The intersections of the $-2\ln\Lambda$ curve with the horizontal lines labelled 1σ and 2σ provide the 68.3% and 95.5% confidence intervals. (b) Summary of the Higgs boson mass measurements from the analysis of $H \to \gamma\gamma$ decays in ATLAS Run 2 data and combined Run 1+Run 2 data presented in this note, compared with the combined Run 1 ATLAS result in the diphoton channel and with the Run 1 measurement by ATLAS and CMS [9] combining diphoton and four leptons channels. The statistical, systematic and total uncertainties are indicated with horizontal yellow-shaded bands, pink-shaded bands and black error bars, respectively. The vertical dashed line and grey shaded band around it indicate the central value and the total uncertainty of the $H \to \gamma\gamma$ ATLAS Run 1+2 measurement, respectively.

A combination is performed with the previous measurement, $m_H = 126.02 \pm 0.43(\text{stat.}) \pm 0.27(\text{syst.})$ GeV, obtained by ATLAS in the diphoton channel using 25 fb^{-1} of proton-proton collisions recorded at $\sqrt{s} = 7$ and 8 TeV during the LHC Run 1 in 2011–2012 [9]. The combination of ATLAS Run 1 and Run 2 results is performed by simultaneously fitting a single m_H parameter on the two datasets. The nominal model including the 14 signal strengths μ_c of the reconstructed categories is used for the Run 2 dataset while two separate signal strengths, one each for production processes involving either Higgs boson couplings to fermions or to vector bosons, are used for the Run 1 dataset. All 16 signal strength parameters are profiled in the combined fit for m_H. Almost all the nuisance parameters, in particular the E_{T}-dependent photon energy scale parameters affected by the linearity measurement and the parameters describing the extrapolation of the energy scale from electrons to photons, are assumed to be uncorrelated between the two measurements due to differences in the reconstruction algorithms and in the calibration procedures and control samples. The $Z \to e^+e^-$ scale uncertainties and part of the resolution uncertainties, estimated in the same way for the two measurements, are considered as fully correlated between the two data-taking periods. The combination with the Run 1 ATLAS measurement in the diphoton channel causes a small shift (+50 MeV) of the central value and a slight reduction (< 10 MeV) of the statistical uncertainty, leading to:

$$m_H = 125.22 \pm 0.11(\text{stat.}) \pm 0.09(\text{syst.}) \text{ GeV} = 125.22 \pm 0.14 \text{ GeV}. \quad (3)$$

The individual ATLAS Run 1 and Run 2 measurements in the diphoton channel and their combination are shown, together with the ATLAS+CMS Run 1 measurement [9] using $H \to \gamma\gamma$ and $H \to 4\ell$ decays, are shown in Figure 3(b).

8 Conclusion

A measurement of the Higgs boson mass in the diphoton channel has been performed using the Run 2 pp collision data recorded by the ATLAS experiment at the CERN Large Hadron Collider at a centre-of-mass energy of 13 TeV, corresponding to an integrated luminosity of 140 fb^{-1}. With respect to a previous measurement in the same decay channel, that was based on a four times smaller dataset at the same energy, this measurement has a systematic (total) uncertainty that is reduced by a factor close to four (three). The reduction in systematic uncertainty is mainly due to an improved photon energy scale calibration, with better energy resolution, and smaller E_{T}-dependent and $e^{\pm} \to \gamma$ extrapolation uncertainties.

The Higgs boson mass is measured to be $m_H = 125.17 \pm 0.14$ GeV. The combination with the Run 1 ATLAS result in the same decay channel yields a value $m_H = 125.22 \pm 0.14$ GeV. With a relative uncertainty of 1.1 per mille, this is currently the most precise measurement of the mass of the Higgs boson from a single channel.

Acknowledgements

We thank CERN for the very successful operation of the LHC, as well as the support staff from our institutions without whom ATLAS could not be operated efficiently.

We acknowledge the support of ANPCyT, Argentina; YerPhI, Armenia; ARC, Australia; BMWFW and FWF, Austria; ANAS, Azerbaijan; CNPq and FAPESP, Brazil; NSERC, NRC and CFI, Canada; CERN; ANID, Chile; CAS, MOST and NSFC, China; Minciencias, Colombia; MEYS CR, Czech Republic; DNRF and DNSRC, Denmark; IN2P3-CNRS and CEA-DRF/IRFU, France; SRNSFG, Georgia; BMBF, HGF and MPG, Germany; GSRI, Greece; RGC and Hong Kong SAR, China; ISF and Benoziyo Center, Israel; INFN, Italy; MEXT and JSPS, Japan; CNRST, Morocco; NWO, Netherlands; RCN, Norway; MEiN, Poland; FCT, Portugal; MNE/IFA, Romania; MESTD, Serbia; MSSR, Slovakia; ARRS and MIZŠ, Slovenia; DSI/NRF, South Africa; MICINN, Spain; SRC and Wallenberg Foundation, Sweden; SERI, SNSF and Cantons of Bern and Geneva, Switzerland; MOST, Taiwan; TENMAK, Türkiye; STFC, United Kingdom; DOE and NSF, United States of America. In addition, individual groups and members have received support from BCKDF, CANARIE, Compute Canada and CRC, Canada; PRIMUS 21/SCI/017 and UNCE SCI/013, Czech Republic; COST, ERC, ERDF, Horizon 2020 and Marie Skłodowska-Curie Actions, European Union; Investissements d'Avenir Labex, Investissements d'Avenir Idex and ANR, France; DFG and AvH Foundation, Germany; Herakleitos, Thales and Aristeia programmes co-financed by EU-ESF and the Greek NSRF, Greece; BSF-NSF and MINERVA, Israel; Norwegian Financial Mechanism 2014-2021, Norway; NCN and NAWA, Poland; La Caixa Banking Foundation, CERCA Programme Generalitat de Catalunya and PROMETEO and GenT Programmes Generalitat Valenciana, Spain; Göran Gustafssons Stiftelse, Sweden; The Royal Society and Leverhulme Trust, United Kingdom.

The crucial computing support from all WLCG partners is acknowledged gratefully, in particular from CERN, the ATLAS Tier-1 facilities at TRIUMF (Canada), NDGF (Denmark, Norway, Sweden), CC-IN2P3 (France), KIT/GridKA (Germany), INFN-CNAF (Italy), NL-T1 (Netherlands), PIC (Spain), ASGC (Taiwan), RAL (UK) and BNL (USA), the Tier-2 facilities worldwide and large non-WLCG resource providers. Major contributors of computing resources are listed in Ref. [38].

Appendix

Table 3 gives the half-width of the smallest invariant mass window containing 68% of the signal events for each analysis category and for the inclusive case.

Figure 4 illustrates the definition of the event categories used for this measurement.

Figure 5 shows the projection of the final fit to the diphoton invariant mass distribution in each category.

Figure 7 shows the measured signal strengths in each reconstructed event category in the nominal fit to the Run 2 data.

Figure 8 shows the best-fit values and uncertainties of the differences Δm_H^i between the mass measured in the category i with respect to the mass measured simultaneously in all other categories.

Figure 10 shows the total systematic uncertainty in the Higgs boson mass from the photon energy scale calibration using the analysis strategy of this article and, respectively, the previous calibration model [35] or the new calibration model [14] with or without the linearity fit to constrain the E_{T}-dependence of the energy scale corrections.

Table 3: The half-width of the smallest invariant mass window containing 68% of the signal events for each analysis category and for the inclusive case.

Category	$\sigma_{68}^{\gamma\gamma}$ [GeV]
U, Central-barrel, high $p_{\mathrm{Tt}}^{\gamma\gamma}$	1.10
U, Central-barrel, medium $p_{\mathrm{Tt}}^{\gamma\gamma}$	1.38
U, Central-barrel, low $p_{\mathrm{Tt}}^{\gamma\gamma}$	1.47
U, Outer-barrel, high $p_{\mathrm{Tt}}^{\gamma\gamma}$	1.24
U, Outer-barrel, medium $p_{\mathrm{Tt}}^{\gamma\gamma}$	1.52
U, Outer-barrel, low $p_{\mathrm{Tt}}^{\gamma\gamma}$	1.75
U, Endcap	1.90
C, Central-barrel, high $p_{\mathrm{Tt}}^{\gamma\gamma}$	1.17
C, Central-barrel, medium $p_{\mathrm{Tt}}^{\gamma\gamma}$	1.51
C, Central-barrel, low $p_{\mathrm{Tt}}^{\gamma\gamma}$	1.68
C, Outer-barrel, high $p_{\mathrm{Tt}}^{\gamma\gamma}$	1.44
C, Outer-barrel, medium $p_{\mathrm{Tt}}^{\gamma\gamma}$	1.82
C, Outer-barrel, low $p_{\mathrm{Tt}}^{\gamma\gamma}$	2.10
C, Endcap	2.23
Inclusive	1.82

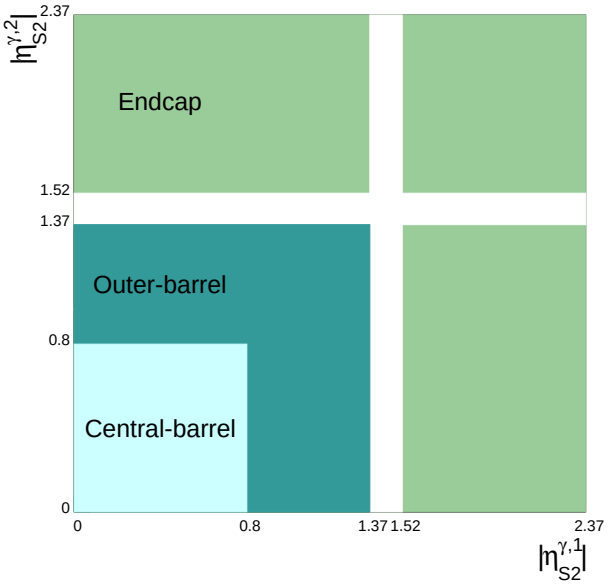

(a)

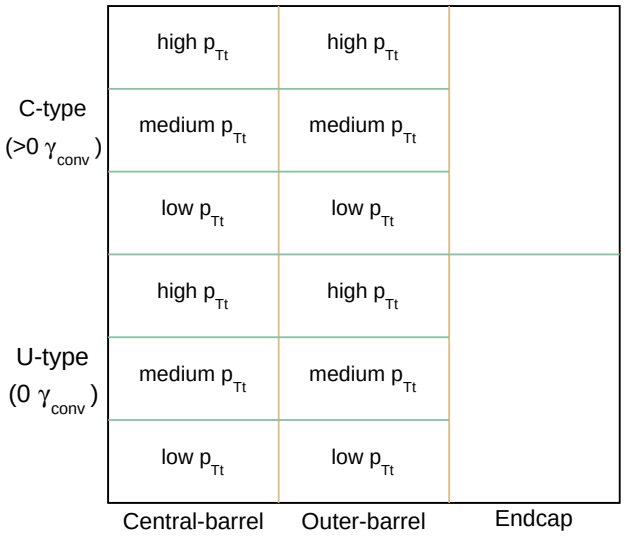

(b)

Figure 4: (a): definition of the three photon pseudorapidity regions used to define the event categories: central barrel (light-blue), outer barrel (blue) and endcap (light green). (b) Illustration of the event categories used for the Higgs boson mass measurement with $H \to \gamma\gamma$ decays.

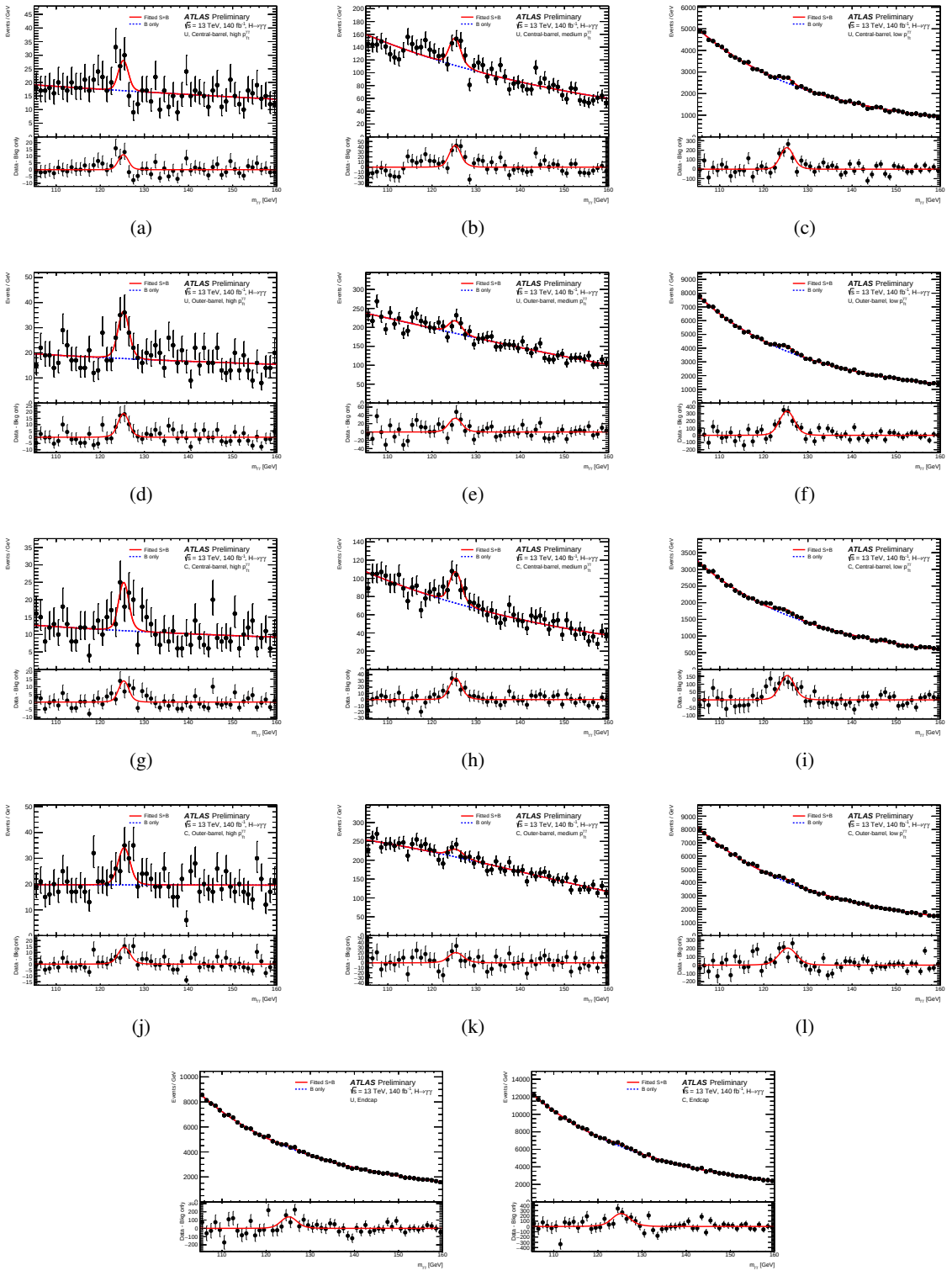

(a) (b) (c)

(d) (e) (f)

(g) (h) (i)

(j) (k) (l)

(m) (n)

Figure 5: Projections of the final fit to the diphoton invariant mass distribution in each category. The style of the figures matches that of Figure 2, but events are not weighted. The background component of the model shown in the plots is represented by an exponential function in Figures 5(a),5(b),5(h) and 5(j), a power-law function in Figures 5(d) and 5(g), while an exponentiated second-order polynomial is used on all other Figures. In addition, the lower panels show the residuals between the data and the fitted background-only model.

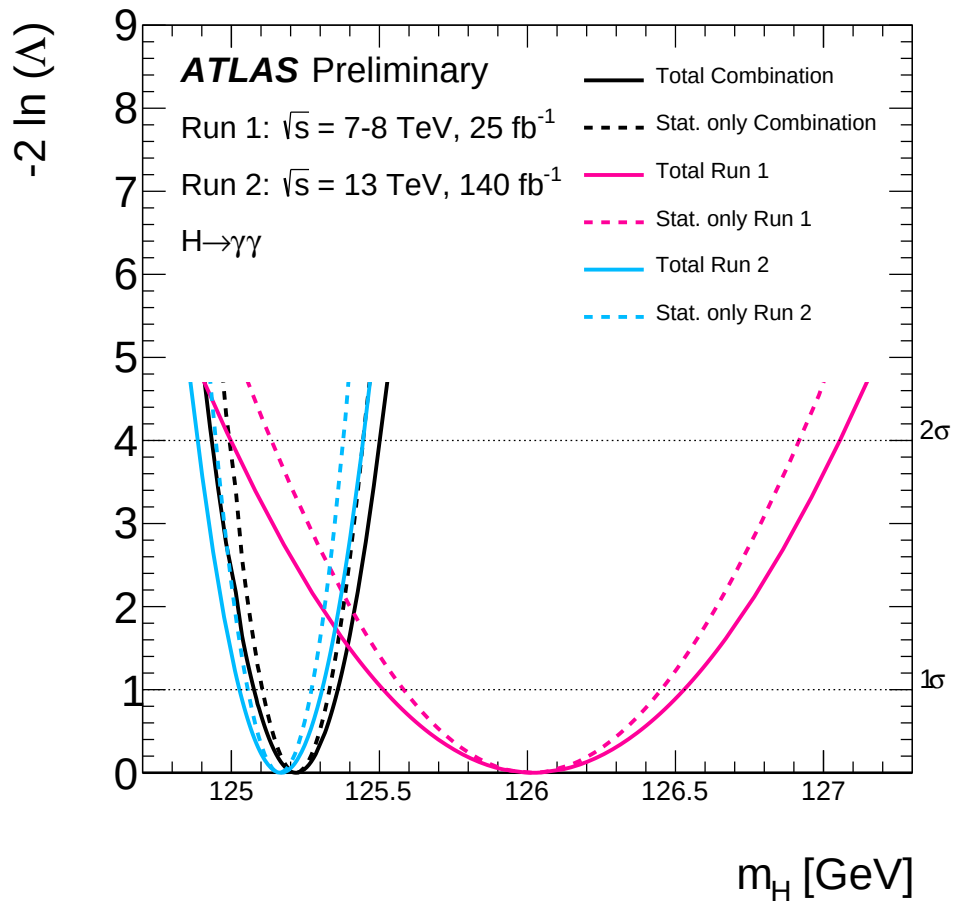

Figure 6: Value of $-2\ln\Lambda$ as a function of m_H for the Run 1 (magenta) and Run 2 (cyan) data and their combination (black), taking into account all uncertainties (solid lines) or only the statistical component (dashed lines).

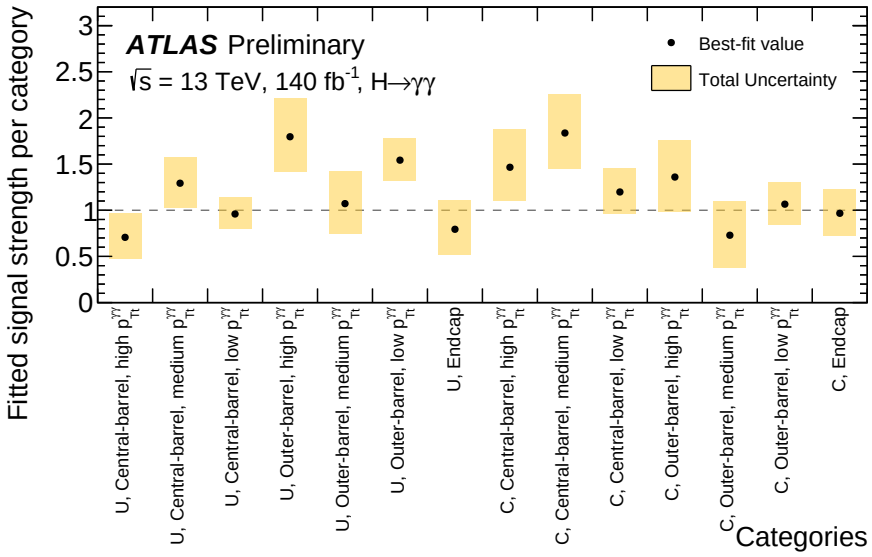

Figure 7: The measured signal strengths in each reconstructed event category in the nominal fit to the Run 2 data.

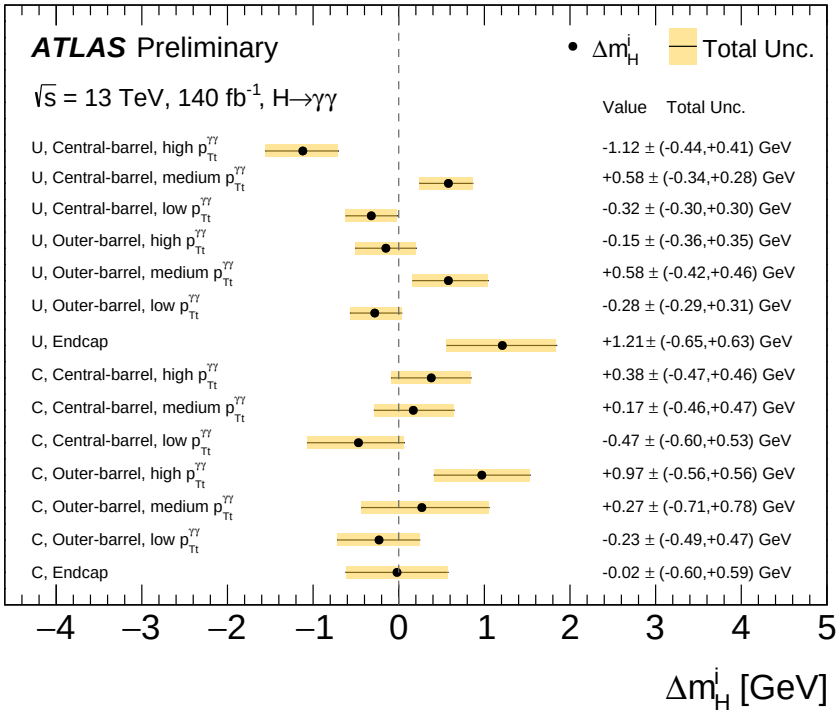

Figure 8: Best-fit values and uncertainties of the differences Δm_H^i between the mass measured in the analysis category i with respect to the mass measured simultaneously in all other analysis categories. For this measurement, the mass in the analysis category under test is parametrised as $m_H^i = m_H + \Delta m_H^i$. The results are obtained from the scan of the modified profile likelihood ratio as a function of Δm_H^i.

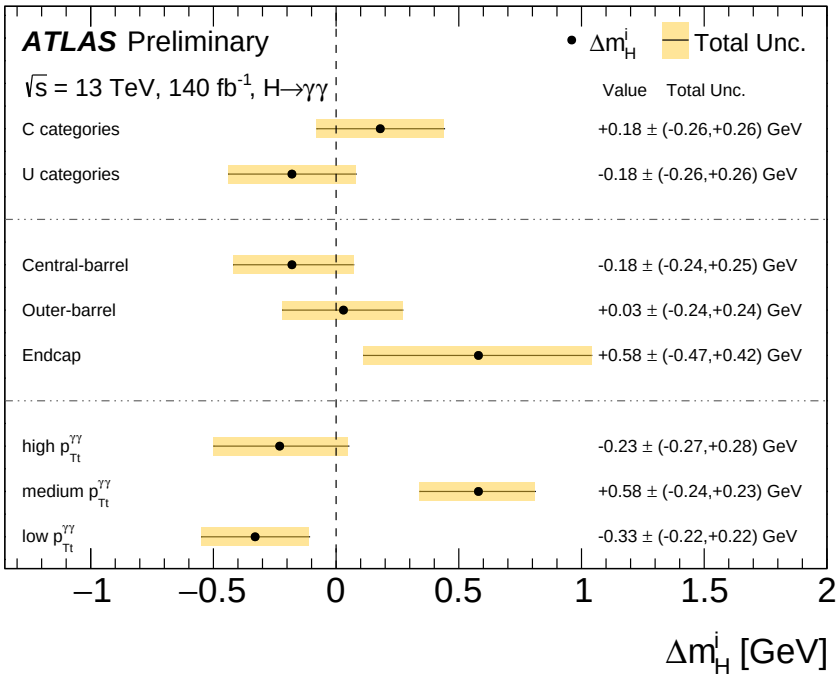

Figure 9: Best-fit values and uncertainties of the differences Δm_H^i between the mass measured in the category i with respect to the mass measured simultaneously in all other categories. For this measurement, the mass in the category under test is parametrised as $m_H^i = m_H + \Delta m_H^i$. The results are obtained from the scan of the modified profile likelihood ratio as a function of Δm_H^i. Three alternative categorisations are considered, based either on the presence or absence of converted photons (top: C-type vs U-type categories), on the photon pseudorapidities (middle: central-barrel vs outer-barrel vs endcap categories), or on the diphoton transverse momentum (bottom: high, medium or low $p_{\mathrm{Tt}}^{\gamma\gamma}$).

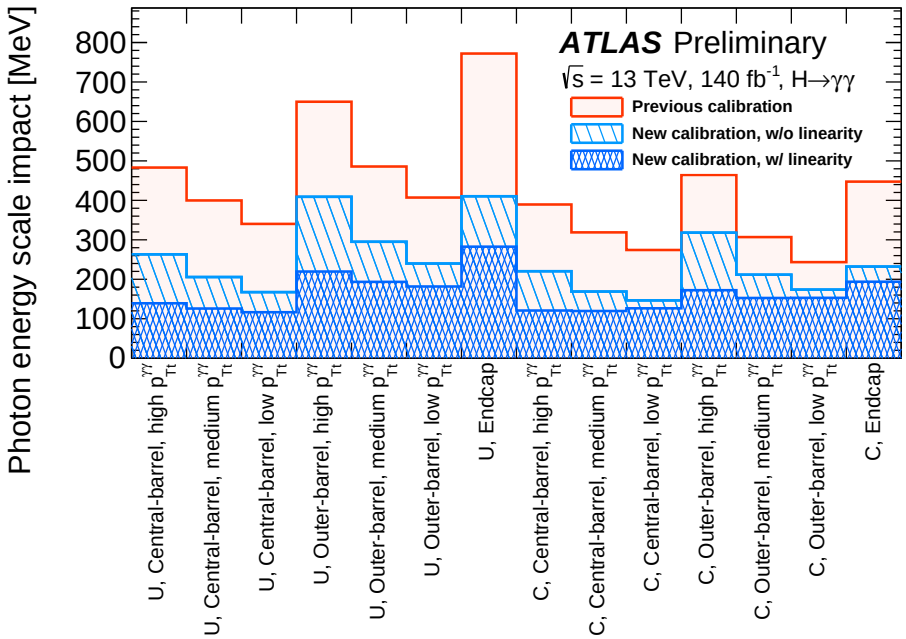

Figure 10: Total systematic uncertainty in the Higgs boson mass from the photon energy scale calibration using the analysis strategy of this article and, respectively, the previous calibration model [35] (light red histogram) or the new calibration model [14] with (light-blue hatched histogram) or without (dark-blue hatched histogram) the linearity fit to constrain the E_{T}-dependence of the energy scale corrections.

References

[1] ATLAS Collaboration, *Observation of a new particle in the search for the Standard Model Higgs boson with the ATLAS detector at the LHC*, Phys. Lett. B **716** (2012) 1, arXiv: 1207.7214 [hep-ex] (cit. on p. 2).

[2] CMS Collaboration, *Observation of a new boson at a mass of 125 GeV with the CMS experiment at the LHC*, Phys. Lett. B **716** (2012) 30, arXiv: 1207.7235 [hep-ex] (cit. on p. 2).

[3] D. de Florian et al., *Handbook of LHC Higgs Cross Sections: 4. Deciphering the Nature of the Higgs Sector*, (2016), arXiv: 1610.07922 [hep-ph] (cit. on pp. 2, 5).

[4] J. Haller et al., *Update of the global electroweak fit and constraints on two-Higgs-doublet models*, Eur. Phys. J. C **78** (2018) 675, arXiv: 1803.01853 [hep-ph] (cit. on p. 2).

[5] M. Sher, *Electroweak Higgs Potentials and Vacuum Stability*, Phys. Rept. **179** (1989) 273 (cit. on p. 2).

[6] G. Degrassi et al., *Higgs mass and vacuum stability in the Standard Model at NNLO*, JHEP **08** (2012) 098, arXiv: 1205.6497 [hep-ph] (cit. on p. 2).

[7] ATLAS Collaboration, *Measurement of the Higgs boson mass from the $H \to \gamma\gamma$ and $H \to ZZ^* \to 4\ell$ channels in pp collisions at center-of-mass energies of 7 and 8 TeV with the ATLAS detector*, Phys. Rev. D **90** (2014) 052004, arXiv: 1406.3827 [hep-ex] (cit. on pp. 2, 3).

[8] CMS Collaboration, *Precise determination of the mass of the Higgs boson and tests of compatibility of its couplings with the standard model predictions using proton collisions at 7 and 8 TeV*, Eur. Phys. J. C **75** (2015) 212, arXiv: 1412.8662 [hep-ex] (cit. on pp. 2, 3).

[9] ATLAS and CMS Collaborations, *Combined Measurement of the Higgs Boson Mass in pp Collisions at $\sqrt{s} = 7$ and 8 TeV with the ATLAS and CMS Experiments*, Phys. Rev. Lett. **114** (2015) 191803, arXiv: 1503.07589 [hep-ex] (cit. on pp. 3, 14).

[10] ATLAS Collaboration, *Measurement of the Higgs boson mass in the $H \to ZZ^* \to 4\ell$ and $H \to \gamma\gamma$ channels with $\sqrt{s} = 13$ TeV pp collisions using the ATLAS detector*, Phys. Lett. B **784** (2018) 345, arXiv: 1806.00242 [hep-ex] (cit. on pp. 3, 5, 7, 8, 10, 11).

[11] CMS Collaboration, *A measurement of the Higgs boson mass in the diphoton decay channel*, Phys. Lett. B **805** (2020) 135425, arXiv: 2002.06398 [hep-ex] (cit. on p. 3).

[12] ATLAS Collaboration, *Measurement of the Higgs boson mass in the $H \to ZZ^* \to 4\ell$ decay channel using 139 fb^{-1} of $\sqrt{s} = 13$ TeV pp collisions recorded by the ATLAS detector at the LHC*, CERN-EP-2022-135 (2022), arXiv: 2207.00320 [hep-ex] (cit. on p. 3).

[13] ATLAS Collaboration, *Electron and photon performance measurements with the ATLAS detector using the 2015–2017 LHC proton–proton collision data*, JINST **14** (2019) P12006, arXiv: 1908.00005 [hep-ex] (cit. on pp. 3, 5, 6, 11).

[14] ATLAS Collaboration, *Electron and photon energy calibration with the ATLAS detector using LHC Run 2 data*, CERN-EP-2023-128 (to be published) (cit. on pp. 3, 5, 6, 10–12, 16, 22).

[15] ATLAS Collaboration, *The ATLAS Experiment at the CERN Large Hadron Collider*, JINST **3** (2008) S08003 (cit. on p. 3).

[16] ATLAS Collaboration, *The ATLAS Collaboration Software and Firmware*, ATL-SOFT-PUB-2021-001, 2021, URL: https://cds.cern.ch/record/2767187 (cit. on p. 4).

[17] ATLAS Collaboration, *Performance of electron and photon triggers in ATLAS during LHC Run 2*, Eur. Phys. J. C **80** (2020) 47, arXiv: 1909.00761 [hep-ex] (cit. on p. 4).

[18] ATLAS Collaboration, *ATLAS data quality operations and performance for 2015–2018 data-taking*, JINST **15** (2020) P04003, arXiv: 1911.04632 [physics.ins-det] (cit. on p. 4).

[19] ATLAS Collaboration, *Luminosity determination in pp collisions at $\sqrt{s} = 13$ TeV using the ATLAS detector at the LHC*, (2022), arXiv: 2212.09379 [hep-ex] (cit. on p. 4).

[20] G. Avoni et al., *The new LUCID-2 detector for luminosity measurement and monitoring in ATLAS*, JINST **13** (2018) P07017 (cit. on p. 4).

[21] ATLAS Collaboration, *Measurement of the properties of Higgs boson production at $\sqrt{s} = 13$ TeV in the $H \to \gamma\gamma$ channel using 139 fb^{-1} of pp collision data with the ATLAS experiment*, CERN-EP-2022-094 (2022), arXiv: 2207.00348 [hep-ex] (cit. on pp. 4, 5, 7, 9).

[22] T. Sjöstrand, S. Mrenna and P. Skands, *A brief introduction to PYTHIA 8.1*, Comput. Phys. Commun. **178** (2008) 852, arXiv: 0710.3820 [hep-ph] (cit. on p. 4).

[23] S. Alioli, P. Nason, C. Oleari and E. Re, *A general framework for implementing NLO calculations in shower Monte Carlo programs: the POWHEG BOX*, JHEP **06** (2010) 043, arXiv: 1002.2581 [hep-ph] (cit. on p. 4).

[24] J. Alwall et al., *The automated computation of tree-level and next-to-leading order differential cross sections, and their matching to parton shower simulations*, JHEP **07** (2014) 079, arXiv: 1405.0301 [hep-ph] (cit. on p. 4).

[25] T. Sjöstrand et al., *An introduction to PYTHIA 8.2*, Comput. Phys. Commun. **191** (2015) 159, arXiv: 1410.3012 [hep-ph] (cit. on p. 5).

[26] ATLAS Collaboration, *The ATLAS Simulation Infrastructure*, Eur. Phys. J. C **70** (2010) 823, arXiv: 1005.4568 [physics.ins-det] (cit. on p. 5).

[27] S. Agostinelli et al., *GEANT4 – a simulation toolkit*, Nucl. Instrum. Meth. A **506** (2003) 250 (cit. on p. 5).

[28] J. Bellm et al., *Herwig 7.1 Release Note*, (2017), arXiv: 1705.06919 [hep-ph] (cit. on p. 5).

[29] E. Bothmann et al., *Event generation with Sherpa 2.2*, SciPost Phys. **7** (2019) 034, arXiv: 1905.09127 [hep-ph] (cit. on p. 5).

[30] ATLAS Collaboration, *The simulation principle and performance of the ATLAS fast calorimeter simulation FastCaloSim*, ATL-PHYS-PUB-2010-013, 2010, URL: https://cds.cern.ch/record/1300517 (cit. on p. 5).

[31] ATLAS Collaboration, *Measurement of Higgs boson production in the diphoton decay channel in pp collisions at center-of-mass energies of 7 and 8 TeV with the ATLAS detector*, Phys. Rev. D **90** (2014) 112015, arXiv: 1408.7084 [hep-ex] (cit. on p. 6).

[32] G. Cowan, K. Cranmer, E. Gross and O. Vitells, *Asymptotic formulae for likelihood-based tests of new physics*, Eur. Phys. J. C **71** (2011) 1554, arXiv: 1007.1727 [physics.data-an] (cit. on pp. 7, 8), Erratum: Eur. Phys. J. C **73** (2013) 2501.

[33] ATLAS Collaboration, *Combined search for the Standard Model Higgs boson in pp collisions at $\sqrt{s} = 7$ TeV with the ATLAS detector*, Phys. Rev. D **86** (2012) 032003, arXiv: 1207.0319 [hep-ex] (cit. on p. 8).

[34] M. Oreglia, *A Study of the Reactions $\psi' \to \gamma\gamma\psi$, Appendix D*, (1980), URL: http://www-public.slac.stanford.edu/sciDoc/docMeta.aspx?slacPubNumber=slac-r-236.html (cit. on p. 8).

[35] ATLAS Collaboration, *Electron and photon energy calibration with the ATLAS detector using 2015–2016 LHC proton–proton collision data*, JINST **14** (2019) P03017, arXiv: 1812.03848 [hep-ex] (cit. on pp. 10, 16, 22).

[36] L. Dixon and M. S. Siu, *Resonance-Continuum Interference in the Diphoton Higgs Signal at the LHC*, Phys. Rev. Lett. **90** (2003) 252001, arXiv: hep-ph/0302233 (cit. on p. 11).

[37] ATLAS Collaboration, *Estimate of the m_H shift due to interference between signal and background processes in the $H \to \gamma\gamma$ channel, for the $\sqrt{s} = 8$ TeV dataset recorded by ATLAS*, ATL-PHYS-PUB-2016-009, 2016, URL: https://cds.cern.ch/record/2146386 (cit. on p. 11).

[38] ATLAS Collaboration, *ATLAS Computing Acknowledgements*, ATL-SOFT-PUB-2021-003, 2021, URL: https://cds.cern.ch/record/2776662 (cit. on p. 15).